PHOTONICS Research

Navigation-grade resonant fiber-optic gyroscope using ultra-simple white-light multibeam interferometry

Shuangxiang Zhao,[1] Qingwen Liu,[1,3] Yuanyuan Liu,[1] Huilian Ma,[2] and Zuyuan He[1,4]

[1]State Key Laboratory of Advanced Communication Systems and Networks, Shanghai Jiao Tong University, Shanghai 200240, China
[2]School of Aeronautics and Astronautics, Zhejiang University, Hangzhou 310027, China
[3]e-mail: liuqingwen@sjtu.edu.cn
[4]e-mail: zuyuanhe@sjtu.edu.cn

Received 17 September 2021; revised 26 November 2021; accepted 17 December 2021; posted 21 December 2021 (Doc. ID 443496); published 1 February 2022

The miniaturization of the gyroscope is critical for spacecrafts, drones, wellbore surveys, etc. The resonant fiber-optic gyroscope (RFOG) is a competitive candidate due to its potential in both miniaturization and high resolution, while its actual performance is well below expectation because of laser-induced noise and complexity. Here we report the first navigation grade RFOG with a bias instability of 0.009°/h and an angle random walk of 0.0093°/$\sqrt{h}$. The results are realized using a fiber resonator with finesse of 63 containing 100-m long fiber. Compared with the traditional RFOGs using narrow-linewidth lasers, the key feature of the proposed RFOG is that it is driven with a broadband light source. A white-light multibeam interference method is proposed to detect the Sagnac effect, representing the simplest scheme of RFOG to date. The complexity caused by multiple feedback loops and coherent noise suppression in traditional RFOG scheme is avoided. The minimal scheme and simple modulation algorithm will also promote the on-chip waveguide gyroscope.

https://doi.org/10.1364/PRJ.443496

1. INTRODUCTION

The fiber-optic gyroscope (FOG) utilizes the Sagnac effect between the two counterpropagating light beams for rotation measurement. As the core device in inertial navigation systems, FOG is indispensably adopted under many extreme environments like aerospace, drones, and wellbore surveys [1,2]. Those applications have a strong demand for the reliability and miniaturization of the gyroscope. The interferometric FOG (IFOG) is the first generation and the only mature type of FOG, in which the Sagnac effect behaves as the phase shift between the two counterpropagating light beams, and the phase shift is detected by the interference of a low-coherence light. The IFOG has a very simple structure known as a "minimal scheme" [3,4], which brings superiority in cost, system simplicity, robustness, and portability over the ring laser gyroscope [5,6] and the advantage of much higher resolution over the microelectromechanical system gyroscope [7,8].

In spite of their great success, high-resolution IFOGs usually employ kilometer-level fiber coil to enlarge the phase shift caused by rotation. The long fiber coil, however, intensifies the thermal ununiformity and leads to the Shupe effect, which would degrade the resolution [9]. By redirecting the light beam into the fiber coil, re-entrant FOG has been proposed as a size-reduced IFOG configuration to relieve the Shupe effect [10,11]. However, the re-entrant FOG is not a very effective option because its actual performance is limited by the optical power loss and the complicated demodulation method. The miniaturization of IFOG remains very challenging.

As the second generation of FOG, the resonant FOG (RFOG) is another potential solution to miniaturization, which employs a high-finesse recirculating fiber ring resonator (FRR) to enhance the Sagnac effect [12,13]. It has the same theoretical resolution as IFOG but with much shorter fiber length, and the nonreciprocity noises such as the Shupe effect can be effectively suppressed with a shorter fiber [2,14] in practice. More attractively, the technology for RFOG is also the most feasible solution to the on-chip gyroscope, in which an optical waveguide resonator replaces the FRR [15–18].

Active research has been dedicated to RFOG [19,20] over the past four decades, but progress has gone very slowly, and the best-reported RFOG has not reached the navigation grade yet [21,22]. Unlike the situation in IFOG, the Sagnac effect in RFOG behaves as the resonant frequency shift of FRR, so, up to date, all the RFOGs use narrow-linewidth lasers to detect the resonant frequency deviation, which introduces serious parasitic noises including backscattering, backreflection,

polarization cross talk, nonlinear Kerr effect, and laser frequency noise [13]. In addition, at least two independent optical frequency locking loops are required to lock the laser to FRR resonances in both clockwise (CW) and counterclockwise (CCW) directions [23]. The extra elements for frequency locking further deteriorate the parasitic noises. In general, the current RFOG technologies lose the simplicity of IFOG, and the complicated system setup results in extra noises and fragility.

Here we have developed a new RFOG readout technique, in which the multibeam interferometry of the low-coherence white-light source is proposed to detect the resonant frequency deviation caused by Sagnac effect. It inherits the simplicity of IFOG with the same "minimal scheme," and the two main problems of traditional RFOGs are avoided. A navigation-grade bias instability (BI) of 0.009°/h and an angle random walk (ARW) of 0.0093°/$\sqrt{\text{h}}$ are obtained with a 100-m fiber length in the demonstrational experiment, which is the first report, we believe, of the RFOG.

2. GYRO PRINCIPLE

A. White-Light Multibeam Interferometry

The setup of the RFOG is shown in Fig. 1. According to multibeam interference, the transmission light electric field (E) of the add-drop FRR has the expression [24]

$$E_{\mathrm{CW}} = F_{\mathrm{CW}}E_0 = \frac{(1-R)e^{i\frac{2\pi\upsilon_{\mathrm{CW}}}{\Delta\upsilon_{\mathrm{FSR}}},\frac{1}{2}}}{1-R\cdot e^{i\frac{2\pi\upsilon_{\mathrm{CW}}}{\Delta\upsilon_{\mathrm{FSR}}}}}E_0,$$

$$E_{\mathrm{CCW}} = F_{\mathrm{CCW}}E_0 = \frac{(1-R)e^{i\frac{2\pi\upsilon_{\mathrm{CCW}}}{\Delta\upsilon_{\mathrm{FSR}}},\frac{1}{2}}}{1-R\cdot e^{i\frac{2\pi\upsilon_{\mathrm{CCW}}}{\Delta\upsilon_{\mathrm{FSR}}}}}E_0. \tag{1}$$

Here the subscripts CW and CCW, respectively, denote the clockwise and counterclockwise directions of the FRR. R is the light-splitting ratio of the fiber couplers, E_0 is the input light electric field, F is the transmission function, υ is the optical frequency, and $\Delta\upsilon_{\mathrm{FSR}}$ is the free spectral range. Due to the Sagnac effect, rotation rate (Ω) will introduce a Sagnac frequency shift (f_{sag}) between F_{CW} and F_{CCW}, which can be expressed as $F_{\mathrm{CCW}}(\upsilon) = F_{\mathrm{CW}}(\upsilon + f_{\mathrm{sag}})$. f_{sag} has the expression [25]

$$f_{\mathrm{sag}} = \frac{D}{n\lambda_0}\Omega, \tag{2}$$

where D is the diameter of the gyro coil and λ_0 is the central wavelength of the light source. Equation (2) means that f_{sag} is a linear indicator to Ω. It is measured by the white-light multibeam interferometry in this paper, as illustrated in the following.

For two counterpropagating single-frequency laser beams (E_{CW} and E_{CCW}), their interferometric signal at the photodetector (PD) is $|E_{\mathrm{CW}} + E_{\mathrm{CCW}}|^2/2$. Considering the low-coherence white-light source as the combination of numerous lasers operating at different frequences, its multibeam interferometric signal (P_{PD}) is the integration of all the frequency components and is expressed as [26]

$$\begin{aligned} P_{\mathrm{PD}} &= \int \frac{|E_{\mathrm{CW}} + E_{\mathrm{CCW}}|^2}{2}\mathrm{d}\upsilon \\ &= \int \left[\frac{|E_{\mathrm{CW}}|^2 + |E_{\mathrm{CCW}}|^2}{2} + \mathrm{Re}(E_{\mathrm{CW}}E_{\mathrm{CCW}}^*)\right]\mathrm{d}\upsilon \\ &= \int |E_0|^2\left[\frac{|F_{\mathrm{CW}}|^2 + |F_{\mathrm{CCW}}|^2}{2} + \mathrm{Re}(F_{\mathrm{CW}}F_{\mathrm{CCW}}^*)\right]\mathrm{d}\upsilon. \end{aligned} \tag{3}$$

Here, the power spectral density of the white light has the expression $|E_0(\upsilon)|^2 = P_{\mathrm{in}}S(\upsilon)$. P_{in} is the total input power and $S(\upsilon)$ is the normalized spectral profile [$\int S(\upsilon)\mathrm{d}\upsilon = 1$]. Using K to denote the transmission loss when the white light passes through the FRR, K can be given as $K = \int S|F_{\mathrm{CW}}|^2\mathrm{d}\upsilon = \int S|F_{\mathrm{CCW}}|^2\mathrm{d}\upsilon = \mathrm{Re}(\int SF_{\mathrm{CW}}F_{\mathrm{CW}}^*\mathrm{d}\upsilon)$. It is a constant only related to the finesse and the cavity loss of the FRR. Therefore, Eq. (3) can be simplified as

$$\begin{aligned} P_{\mathrm{PD}} &= KP_{\mathrm{in}}[1 + R(f_{\mathrm{sag}})], \\ R(f_{\mathrm{sag}}) &\overset{\mathrm{def}}{=} \frac{\mathrm{Re}(\int SF_{\mathrm{CW}}F_{\mathrm{CCW}}^*\mathrm{d}\upsilon)}{K}. \end{aligned} \tag{4}$$

Here, the $R(f_{\mathrm{sag}})$ is a normalized function, denoting the correlation between F_{CW} and F_{CCW}. If the RFOG is static, F_{CW} and F_{CCW} overlap exactly in the spectrum, and the correlation function $R(f_{\mathrm{sag}})$ reaches its maximum of 1. If the RFOG rotates, F_{CW} and F_{CCW} are mismatched, and $R(f_{\mathrm{sag}})$ decreases. The combination of Eqs. (2) and (4) directly links the multibeam interference P_{PD} with f_{sag} and Ω, and it is the basic working scheme of the proposed RFOG.

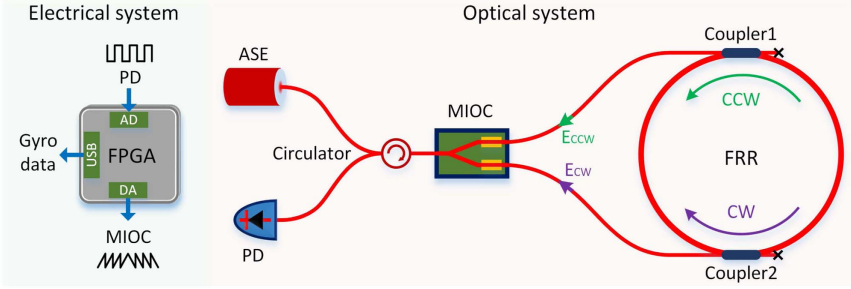

Fig. 1. RFOG setup. ASE, amplified spontaneous emission; PD, photodetector; FPGA, field programmable gate array; MIOC, multifunction integrated-optics chip; FRR, fiber ring resonator; CW, clockwise; CCW, counterclockwise; AD, analog-to-digital; DA, digital-to-analog. Different from traditional IFOGs based on the minimal scheme, the long fiber coil is replaced with a high-finesse FRR. A photograph of the RFOG setup is also provided in Fig. 8 in Appendix A.

B. Simulation and Experiment Demonstration

In the simulation, the spectral profile $S(\upsilon)$ is assumed to be rectangular for simplicity. The spectral bandwidth is set to 4 THz, centering at 193 THz, much larger than the $\Delta\upsilon_{\mathrm{FSR}}$ of the FRR. Under several values of finesse ($\mathcal{F}$), the relationship curves between the normalized P_{PD} and the f_{sag} are computed, as plotted in Fig. 2(a). The simulation curve appears as a Lorentzian resonance, and it is the result of the proposed white-light multibeam interferometry. It has to be pointed out that it is not the actual resonance of FRR. Despite the similar appearance, its finesse is found to be a half of the actual FRR finesse ($\mathcal{F}$). Because of only focusing on a small range of f_{sag} [$|f_{\mathrm{sag}}| < \Delta\upsilon_{\mathrm{FSR}} \ll$ bandwidth of $S(\upsilon)$], it is found that the simulated curves are not affected by the spectral profile and bandwidth of the light source.

Afterwards, an experiment is carried out to demonstrate the proposed white-light multibeam interferometry. In the experiment, the FRR in Fig. 1 is composed of two 98:2 couplers and a fiber coil. The fiber length and diameter of the coil are ~100 m and 140 mm, respectively. The round-trip loss of the cavity is measured to be 0.268 dB. The RFOG is based on panda-type polarization-maintaining (PM) fiber to minimize polarization-related noises. By using an acousto-optic frequency shifter and a narrow-linewidth laser to scan the FRR spectrum, the full width at half-maximum (FWHM) and the $\Delta\upsilon_{\mathrm{FSR}}$ of the FRR resonance are measured to be 30.5 kHz and 1.918 MHz, respectively, corresponding to a finesse of 63.

A multifunction integrated-optics chip (MIOC) is adopted here for light splitting and combining, polarization filtering, and phase modulation. The MIOC is based on $LiNbO_3$, and its half-wave voltage (V_π) is 3.99 V. The light source of the system is an amplified spontaneous emission (ASE) source based on erbium-doped fiber. Its bandwidth is ~35 nm, centering at 1550 nm. Its power is set to 100 mW in the following experiments. In navigation-grade IFOGs, it is a most commonly used source because of its high stability and power. The PD (Thorlabs, PDA10CS-EC) is based on InGaAs and is working at the C band. Its bandwidth ranges from 0 Hz to 1 MHz, and it has adjustable gain.

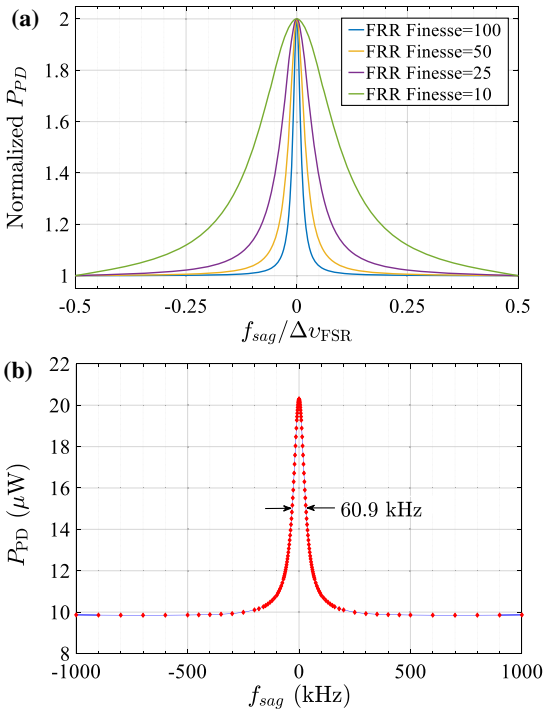

Fig. 2. (a) Simulation analysis and (b) experimental demonstration of Eq. (4). They are the outputs of the proposed white-light multibeam interferometry and are defined as the response curves of the proposed RFOG.

By driving the MIOC with opposite sawtooth waveforms at its two arms, an equivalent f_{sag} can be introduced between the CW and CCW directions (more details on the f_{sag} introducing scheme can be found in Appendix A). Therefore, an experimental curve of Eq. (4) can be obtained by setting the f_{sag} at a series of discrete values and acquiring the corresponding P_{PD}, as shown by the red dots in Fig. 2(b). The blue curve connects the adjacent dots and outlines the curve profile. Its FWHM is 60.9 kHz, corresponding to a halved finesse of 31.5 versus the real FRR finesse. The experiment and the simulation results are in good accordance.

According to the results in Figs. 2(a) and 2(b), the PD receives maximal power P_{PD} if no rotation is applied to the FRR, and it declines sharply if the FRR rotates. The curve in Fig. 2(b) is defined as the response curve of the RFOG. Different from traditional RFOGs, where CW and CCW directions need independent and complicated interrogation systems, the proposed RFOG has a much simpler working scheme. Also unlike the cosine response curve of IFOG [2], the response curve of the RFOG appears as a sharp peak due to multibeam interference, and thus it has improved sensitivity to rotation.

C. RFOG Modulation and Demodulation

The RFOG readout is based on utilizing the property of the response curve in Fig. 2(b). Because of the symmetry of the response curve, modulation techniques are necessary to discriminate between the positive/negative f_{sag}, so as to distinguish the rotation direction. The details of the modulation process are shown in Fig. 3. If there is no modulation and rotation, $P_{\mathrm{PD}}(f_{\mathrm{sag}}) = P_{\mathrm{PD}}(0) \approx 20\ \mu\mathrm{W}$, corresponding to the peak value of the response curve in Fig. 2(b). Because the frequency is the derivative of the phase with time, if the MIOC is driven with upward sawtooth wave (frequency, 21 kHz; peak amplitude, V_π) at the CW arm and the opposite at the CCW arm, a positive frequency bias ($f_{\mathrm{mod}} = 21$ kHz) is introduced to the f_{sag}, and the output of the PD decreases to $P_{\mathrm{PD}}(f_{\mathrm{mod}})$. Afterwards, opposite sawtooth waves are applied to introduce a negative frequency bias $-f_{\mathrm{mod}}$ and the output of the PD becomes $P_{\mathrm{PD}}(-f_{\mathrm{mod}})$.

In the modulation, the f_{mod} alternately changes between ± 21 kHz with a rate of 500 Hz. The variation of P_{PD} during the f_{mod} switching is defined as the error signal $e = P_{\mathrm{PD}}(f_{\mathrm{mod}}) - P_{\mathrm{PD}}(-f_{\mathrm{mod}})$. If there is no rotation, considering the axial symmetry of P_{PD}, e is equal to 0. If a rotation rate is applied and an f_{sag} is introduced, the error signal becomes

$$\begin{aligned} e &= P_{\mathrm{PD}}(f_{\mathrm{mod}} + f_{\mathrm{sag}}) - P_{\mathrm{PD}}(-f_{\mathrm{mod}} + f_{\mathrm{sag}}) \\ &= P_{\mathrm{PD}}(f_{\mathrm{mod}} + f_{\mathrm{sag}}) - P_{\mathrm{PD}}(f_{\mathrm{mod}} - f_{\mathrm{sag}}). \end{aligned} \tag{5}$$

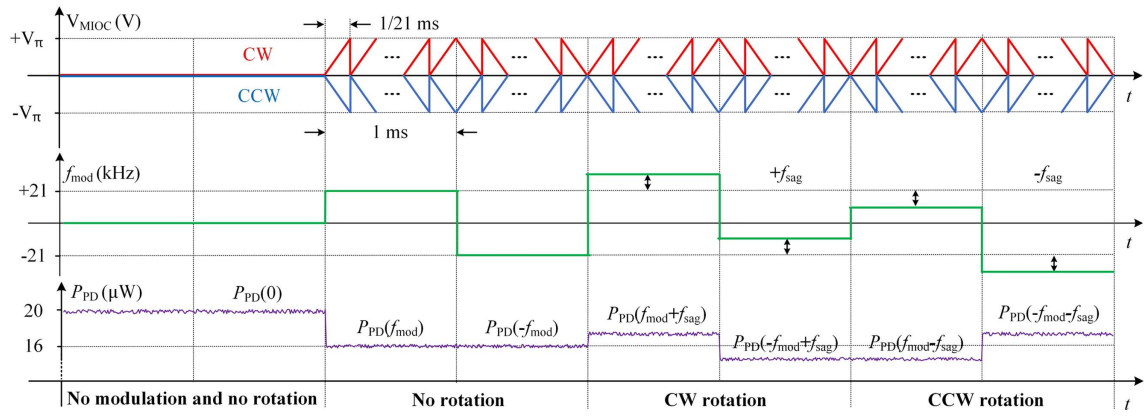

Fig. 3. Modulation signals and the corresponding P_{PD} in different gyro states. V_{MIOC}, voltage applied on the MIOC; V_π, half-wave voltage; f_{mod}, modulated frequency bias.

In the gyro uses, rotation-induced f_{sag} is usually very small ($f_{sag} \ll$ FWHM). Therefore, Eq. (5) can be simplified as

$$e = 2(P'_{PD}|_{f_{mod}})f_{sag} = 2KP_{in}(R'|_{f_{mod}})f_{sag}, \quad f_{sag} \approx 0, \tag{6}$$

where $P'_{PD}|_{f_{mod}}$ and $R'|_{f_{mod}}$ denote the derivative of $P_{PD}(f_{sag})$ and $R(f_{sag})$ at the point $f_{sag} = f_{mod}$, respectively. Equation (6) indicates that error signal e is a linear indicator to f_{sag} and Ω. To maximize the e-to-f_{sag} coefficient and to improve the RFOG sensitivity, f_{mod} should be tuned at the steepest edges of the response curve.

A field programmable gate array (FPGA, NI 7855R) module with integrated analog-to-digital (AD) and digital-to-analog (DA) converters is adopted for P_{PD} acquisition, f_{sag} modulation, and e calculation, as shown in Figs. 1 and 4(a). The FPGA multiplies the P_{PD} and the modulation square ($\pm f_{mod}$) with a mixer. The mixer output passes through a low-pass filter (LPF, 20 Hz), and the error signal e is generated referenced to the average input power P_{in}. After these algorithm operations, e is irrelevant to the power level, and it has no unit. Similar to Fig. 2(b), at some discrete values of f_{sag}, e is recorded, as shown by the red dots in Fig. 4(b). This curve is antisymmetric and it crosses zero if no rotation exists, so the rotation direction can be distinguished. At the central region, e is proportional to f_{sag}, with an e-to-f_{sag} coefficient of 1/(7600 Hz). By using a high-precision rotating platform, the Ω-to-f_{sag} coefficient is tested to be 3.4°/(h · Hz). After the calibration of these scaling factors, the rotation signal can be successfully recovered from P_{PD}, and the RFOG gets ready for measurement.

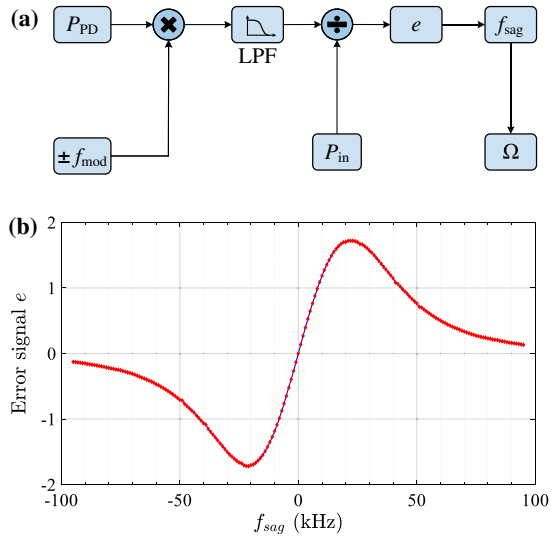

Fig. 4. (a) Demodulation process in the FPGA; (b) measured error signal versus f_{sag}. LPF, low-pass filter.

3. GYRO TEST

The proposed RFOG is first adopted for the rotation test with the high-resolution rotating platform (TD-320), whose nominal rotation resolution and range are 0.0001°/s and >500°/s, respectively. A sinusoidal rotation rate (10°/h, 0.01 Hz) is applied to the RFOG. At the same time, the FPGA records the error signal and recovers the rotation. The rotation data are downsampled to 1 Sa/s via averaging and are plotted in Fig. 5(a), where the sine rotation rate is well recovered. Then the rotation rate is decreased to 1°/h, and Fig. 5(b) is obtained. The recovered sinusoidal curves prove that the resolution of the proposed RFOG is better than 1°/h in the bandwidth of 1 Hz.

The RFOG is then horizontally placed in a sealed box for a static test, where the temperature fluctuation is about 0.4 K/h. In this case, the RFOG is only subjected to the Earth's rotation, which is 7.8°/h at the testing site (Shanghai, China). The gyro data recorded in 35,000 s are shown in Fig. 5(c). The output has a bias around −4.5°/h, which may be attributed to the nonreciprocity of couplers [27]. When the RFOG is turned over to sense the opposite of the Earth's rotation, the bias changes from −4.5°/h to −20.1°/h. The bias difference is twice the Earth's rotation rate. As shown in Fig. 5(c), the dominating gyro noise has the white-noise characteristics. After averaging with a moving window of 1000 s, the long-term bias drift emerges, as shown in Fig. 5(d). Figure 5(e) plots the power spectral density

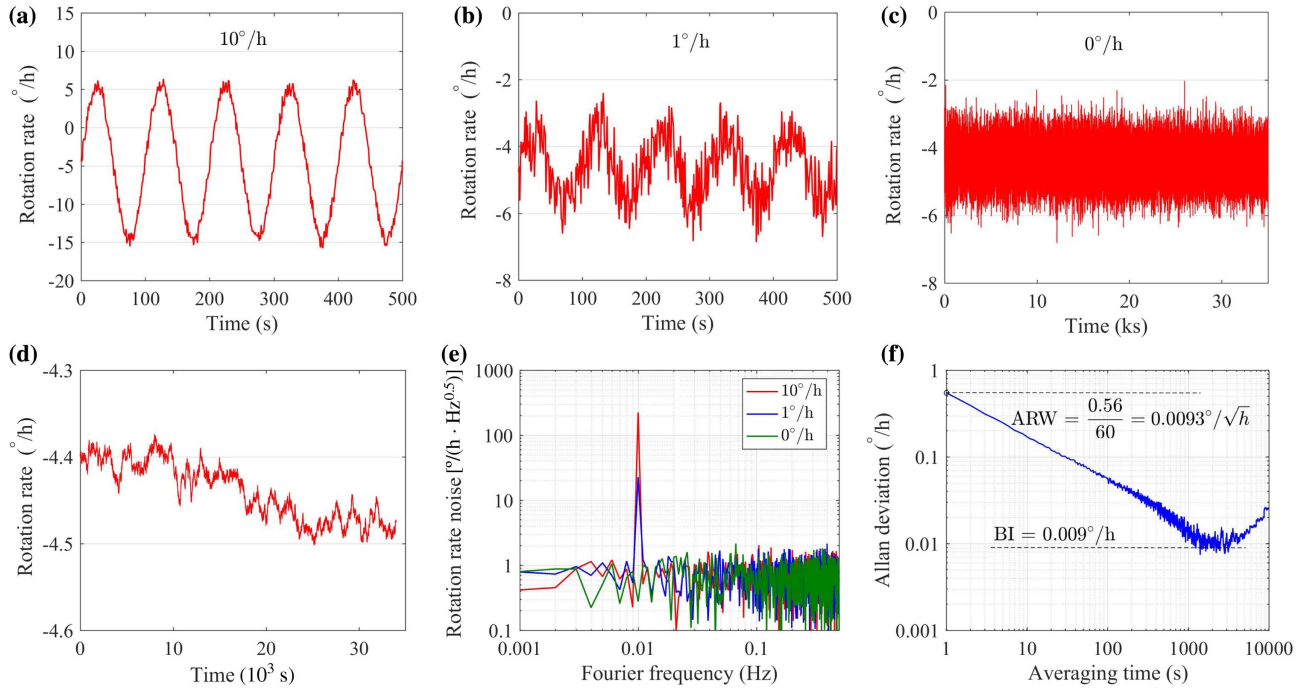

Fig. 5. Test results of the RFOG. Gyro readout under sinusoidal rotation of (a) 10°/h, (b) 1°/h, and (c) 0°/h; (d) moving average of the static test data in (c) with a time window of 1000 s; (e) spectral power density of the results in (a)–(c); (f) Allan deviation of the static test data in (c).

of the gyro data in Figs. 5(a)–5(c). The peaks correspond to the applied rotation signals, and the noise floor is generally around $0.69°/(h \cdot Hz^{0.5})$.

The overlapping Allan deviation of the 35,000-s gyro data is calculated and is shown in Fig. 5(f) [28]. An ARW of $0.0093°/\sqrt{h}$ and a BI of 0.009°/h can be read out from it, which demonstrates that the resolution of the proposed RFOG has reached the navigation grade. In this demo experiment, the RFOG works in an open-loop configuration, so the linear region of the error signal curve in Fig. 4(b) restrains the measurement range of f_{sag} to be about ±15 kHz, corresponding to a rotation rate of ±14°/s. Table 1 lists all the key parameters of the RFOG during the test. This RFOG is also compatible with a closed-loop operation. By adding a feedback control loop to adjust the frequency shift of the MIOC, the rotation-induced f_{sag} can be well compensated so as to null the error signal. The closed-loop configuration can further extend the measurement range and stabilize the gyro bias [29].

Table 1. Parameters of the RFOG

Parameter	Value	Unit
BI	0.009	°/h
ARW	0.0093	°/h
Scale factor	3.4	°/(h · Hz)
Sampling rate	20	Sa/s
Measurement range	±14	°/s
Fiber length (L)	~100	m
Diameter (D)	140	mm
Finesse ($\mathcal{F}$)	63	–
Power at detector (P_{PD})	~16	μW

4. NOISE ANALYSIS

A. Shot-Noise Limited Resolution

The resolution of RFOG is ultimately limited by the shot noise at the detector, which is given by [16,30]

$$\Omega_{min} = \frac{2\lambda_0 c}{L \cdot \mathcal{F} \cdot D}\sqrt{\frac{e_c}{\pi R_D P_{PD} \tau}}, \tag{7}$$

where c is the velocity of light in vacuum, R_D is the responsivity of the PD, e_c is the electron charge, and τ is the integration time. Using the parameters listed in Table 1 and the calculation process in Ref. [16], the shot-noise limited resolution Ω_{min} of the proposed RFOG is calculated to be 0.016°/h at the integration time (τ) of 1 s. According to Fig. 5(f), the demonstrated rotation resolution is 0.56°/h at 1 s. Therefore, there is still ~15 dB space for resolution improvement.

B. RIN-Induced ARW Noise

The noises of gyros are typically classified into two types: short-term ARW noise and long-term nonreciprocity-induced bias drift. In Fig. 5(f), the turning point of Allan deviation appears at an averaging time of ~3000 s, proving that short-term ARW noise is dominating in this RFOG. Therefore, noise analysis on the ARW is necessary to explore the full potential of the proposed RFOG. Since the rotation signal is read from light intensity at the PD, the relative intensity noise (RIN) of P_{PD} is the main contributor to ARW noise and is investigated. Usually, relative to the fundamental shot noise, the RIN induced by the ASE source (know/n as excess RIN) is much higher [31].

In the excess RIN analysis, modulation on the MIOC is turned off, and P_{PD} is adjusted to 16 μW. The RIN of P_{PD} is recorded by the FPGA and is plotted as the red curve in Fig. 6. The excess RIN mostly originates from the random beat of different frequencies of the broadband light [32,33]. Because of the spectral shaping effect of the FRR, the RIN of P_{PD} rises around the frequency of multiple free spectral range (such as 0 Hz and 1.918 MHz). For comparison, the blue curve depicts the RIN of input ASE light (P_{in}), which has a flat noise floor in the frequency domain. Due to the spectral shaping of the FRR, the red curve has higher noise at low frequency and lower noise at high frequency. At the RFOG working frequency of 21 kHz, the rising RIN floor of P_{PD} is responsible for the ARW noise in Fig. 5(f) ($0.0093°/\sqrt{h}$). Since the RIN floor of P_{in} (blue curve) is about 9 dB lower, a lower ARW of $0.0033°/\sqrt{h}$ can be obtained, if without the unwanted spectral shaping effect.

On the other hand, the spectral shaping effect also has positive utilization to suppress the ARW noise [33,34]. By inserting another fiber resonator after the ASE source to reshape the spectra of P_{in} and P_{PD}, a series of RIN notches can be introduced to reduce the RIN floor at the point of working frequency [33]. Except for the spectral shaping method, many other RIN suppression techniques have been developed for IFOG to suppress the ARW noise, such as optical or electrical subtraction [32,35], quadrature demodulation [36], and light depolarization before photodetection [37]. Most of them are compatible with this novel RFOG. So, better ARW performance can be expected to approach the shot-noise limited resolution.

C. Nonreciprocity Noises

Other than ARW noise, nonreciprocity-induced long-term bias drift is another important factor of BI. These nonreciprocities originate from unwanted backreflection, backscattering, polarization cross talk, the Kerr effect, the Shupe effect, etc. [13]. These nonreciprocity noises significantly degrade the performance of traditional RFOG systems because of the employment of high-coherence lasers. However, they are well mitigated in this paper by the use of low-coherence light source and the minimal scheme.

The polarization cross talk in the proposed RFOG is suppressed in the following actions: first, the adoption of PM fiber minimizes the polarization fluctuations while light circulates

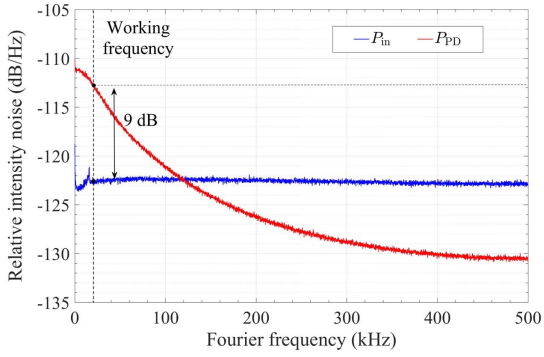

Fig. 6. RIN of P_{PD} and P_{in}. The working frequency of the RFOG is 21 kHz.

Table 2. Comparison between the Proposed RFOG and Traditional FOGs

	Traditional IFOGs	Traditional RFOGs	Proposed RFOG
Light source	White light	Laser	White light
Sensing element	Fiber coil	FRR	FRR
Resolution	High	Low	Medium
Size	Large	Small	Small
Complexity	Low	High	Low

inside the FRR. In addition, the MIOC has integrated polarizers to ensure the polarization consistency between the input and output light. The high polarization extinction ratio of the PM fiber and the MIOC makes the whole system operate stably in single polarization. Further, thanks to the low-coherence nature of the broadband light, the residual interference noise between two orthogonal polarizations is well mitigated [38]. The efficiency of these polarization-suppression actions (polarizer, PM fiber, and low-coherence source) has been widely demonstrated in numerous navigation-grade IFOGs.

The nonlinear Kerr effect is proportional to the intensity imbalance between the CW and CCW light waves. According to the analysis in Ref. [9], it can also be substantially weakened through the utilization of a low-coherence source.

The Shupe effect originates from thermal ununiformity along the long fiber coil. In most IFOG systems, the fiber coil is commonly fabricated with elaborate winding and packaging techniques to mitigate the thermal ununiformity [39,40]. The residual Shupe effect, however, limits the further resolution improvement of IFOG. Here, the equivalent length of the RFOG is quite long (~6300 m) considering its finesse of 63. However, the RFOG "packages" the 6300-m equivalent length into an actual size of only ~100 m in the way of optical recirculation and resonance. Compared with the elaborate winding of IFOG coil, it is obviously a more effective approach. Therefore, the RFOG has inherent insensitivity to the thermal-related Shupe effect due to its compact actual size.

5. CONCLUSION

In summary, we present the first navigation-grade RFOG with the simplest readout scheme to date. As shown in Table 2, compared with traditional IFOGs and RFOGs, the proposed RFOG utilizes a low-coherence white-light source, high-finesse FRR, and the minimal scheme. It combines the key advantages of conventional IFOGs and RFOGs such as ultralow complexity and compact size. In the experiment, an ARW of $0.0093°/\sqrt{h}$ and a BI of 0.009°/h have been achieved with a 100-m fiber coil. It shows great potential in both high resolution and on-chip integration.

APPENDIX A

The MIOC integrates two phase modulators at the CW and CCW arms, respectively, and they are driven with opposite voltage to work in the push–pull mode. By applying sawtooth waveforms to the MIOC, the MIOC works as two frequency shifters, since frequency is the derivative of phase. Figure 7(a)

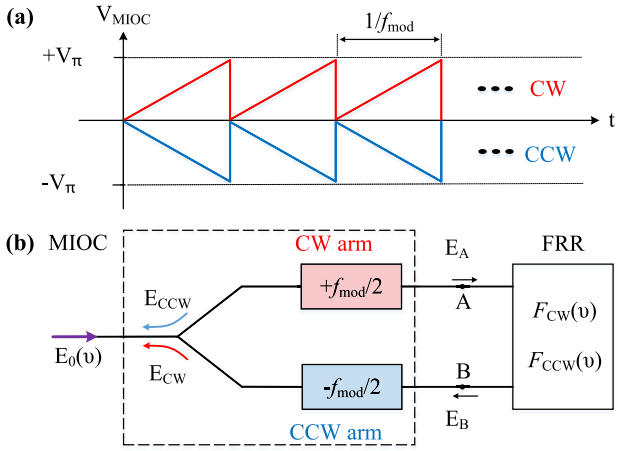

Fig. 7. Scheme of introducing equivalent Sagnac frequency via sawtooth modulation. (a) Modulation waveforms at two arms of the MIOC; (b) modulation process and scheme.

shows the applied sawtooth modulation waveforms. The sawtooth slope is $V_\pi f_{\mathrm{mod}}$ at the CW arm and $-V_\pi f_{\mathrm{mod}}$ at the CCW arm, which would introduce $\pm\frac{f_{\mathrm{mod}}}{2}$ frequency shifts at the CW and CCW arms, respectively.

The modulation process and scheme of the MIOC are shown in Fig. 7(b). The input light electric field is $E_0(\upsilon)$. After the light splitting and the CW frequency shifter $(+\frac{f_{\mathrm{mod}}}{2})$, E_A (the light electric field at point A) has the expression $E_A = \frac{\sqrt{2}}{2}E_0(\upsilon - \frac{f_{\mathrm{mod}}}{2})$. Then, after passing through the FRR, E_B (the light electric field at point B) has the expression $E_B = F_{\mathrm{CW}}E_A = \frac{\sqrt{2}}{2}F_{\mathrm{CW}}(\upsilon)E_0(\upsilon - \frac{f_{\mathrm{mod}}}{2})$. Further, E_B passes through the CCW frequency shifter $(-\frac{f_{\mathrm{mod}}}{2})$ and the light combiner, and the CW light field (E_{CW}) has the expression

$$E_{\mathrm{CW}} = \frac{1}{2}F_{\mathrm{CW}}\left(\upsilon + \frac{f_{\mathrm{mod}}}{2}\right)E_0(\upsilon). \tag{A1}$$

For the same reason, the CCW light field (E_{CCW}) has the expression

$$E_{\mathrm{CCW}} = \frac{1}{2}F_{\mathrm{CCW}}\left(\upsilon - \frac{f_{\mathrm{mod}}}{2}\right)E_0(\upsilon). \tag{A2}$$

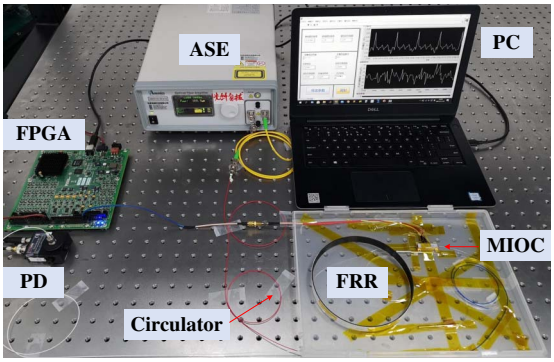

Fig. 8. Photograph of the RFOG system. PC, personal computer.

Equations (A1) and (A2) indicate that an equivalent Sagnac frequency f_{mod} can be introduced between the CW and CCW directions by driving the MIOC with the sawtooth waveform plotted in Fig. 7(a). It is the theoretical basis of the RFOG modulation in this paper.

Funding. National Key Research and Development Program of China (2018YFC1503703); National Natural Science Foundation of China (61620106015, 61875121, 61975116).

Acknowledgment. S. X. Zhao proposed the method, performed the experiment, and wrote the draft of the paper; Q. W. Liu, H. L. Ma, and Z. Y. He edited the paper and assisted in improving the sensor performance; S. X. Zhao and Y. Y. Liu analyzed the data; Z. Y. He supervised the project.

Disclosures. The authors declare no conflicts of interest.

Data Availability. Data underlying the results presented in this paper are not publicly available at this time but may be obtained from the authors upon reasonable request.

REFERENCES

1. E. J. Post, "Sagnac effect," Rev. Mod. Phys. **39**, 475–493 (1967).
2. H. C. Lefevre, *The Fiber-Optic Gyroscope*, 2nd ed. (Artech House, 2014).
3. R. Luo, Y. Li, S. Deng, C. Peng, and Z. Li, "Effective suppression of residual coherent phase error in a dual-polarization fiber optic gyroscope," Opt. Lett. **43**, 815–818 (2018).
4. X. S. Yao, H. Xuan, X. Chen, H. Zou, X. Liu, and X. Zhao, "Polarimetry fiber optic gyroscope," Opt. Express **27**, 19984–19995 (2019).
5. W. Chow, J. Gea-Banacloche, L. Pedrotti, V. Sanders, W. Schleich, and M. Scully, "The ring laser gyro," Rev. Mod. Phys. **57**, 61–104 (1985).
6. Y.-H. Lai, M.-G. Suh, Y.-K. Lu, B. Shen, Q.-F. Yang, H. Wang, J. Li, S. H. Lee, K. Y. Yang, and K. Vahala, "Earth rotation measured by a chip-scale ring laser gyroscope," Nat. Photonics **14**, 345–349 (2020).
7. M. N. Armenise, C. Ciminelli, F. Dell'Olio, and V. M. Passaro, *Advances in Gyroscope Technologies* (Springer, 2010).
8. K. Liu, W. Zhang, W. Chen, K. Li, F. Dai, F. Cui, X. Wu, G. Ma, and Q. Xiao, "The development of micro-gyroscope technology," J. Micromech. Microeng. **19**, 113001 (2009).
9. I. A. Andronova and G. B. Malykin, "Physical problems of fiber gyroscopy based on the Sagnac effect," Phys. Usp. **45**, 793–817 (2002).
10. C.-Y. Liaw, Y. Zhou, and Y.-L. Lam, "Characterization of an open-loop interferometric fiber-optic gyroscope with the Sagnac coil closed by an erbium-doped fiber amplifier," J. Lightwave Technol. **16**, 2385–2392 (1998).
11. Z. Hu, Y. Zhang, Z. Pan, and Q. Tang, "Digital closed-loop re-entrant fiber-optic rotation sensor with amplified Sagnac loop," IEEE Photon. Technol. Lett. **12**, 1040–1042 (2000).
12. R. Carroll, C. Coccoli, D. Cardarelli, and G. Coate, "The passive resonator fiber optic gyro and comparison to the interferometer fiber gyro," Proc. SPIE **719**, 169–177 (1987).
13. H. Ma, J. Zhang, L. Wang, and Z. Jin, "Development and evaluation of optical passive resonant gyroscopes," J. Lightwave Technol. **35**, 3546–3554 (2016).
14. D. M. Shupe, "Thermally induced nonreciprocity in the fiber-optic interferometer," Appl. Opt. **19**, 654–655 (1980).
15. K. Suzuki, K. Takiguchi, and K. Hotate, "Monolithically integrated resonator microoptic gyro on silica planar lightwave circuit," J. Lightwave Technol. **18**, 66–72 (2000).

16. H. Ma, J. Zhang, L. Wang, Y. Lu, D. Ying, and Z. Jin, "Resonant micro-optic gyro using a short and high-finesse fiber ring resonator," Opt. Lett. **40**, 5862–5865 (2015).
17. W. Liang, V. S. Ilchenko, A. A. Savchenkov, E. Dale, D. Eliyahu, A. B. Matsko, and L. Maleki, "Resonant microphotonic gyroscope," Optica **4**, 114–117 (2017).
18. P. P. Khial, A. D. White, and A. Hajimiri, "Nanophotonic optical gyroscope with reciprocal sensitivity enhancement," Nat. Photonics **12**, 671–675 (2018).
19. X. Wang, Z. He, and K. Hotate, "Reduction of polarization-fluctuation induced drift in resonator fiber optic gyro by a resonator with twin 90° polarization-axis rotated splices," Opt. Express **18**, 1677–1683 (2010).
20. H. Li, Y. Lin, L. Liu, H. Ma, and Z. Jin, "Signal processing improvement of passive resonant fiber optic gyroscope using a reciprocal modulation-demodulation technique," Opt. Express **28**, 18103–18111 (2020).
21. M. Smiciklas, G. Sanders, L. Strandjord, W. Williams, E. Benser, S. Ayotte, and F. Costin, "Development of a silicon photonics-based light source for compact resonator fiber optic gyroscopes," in *DGON Inertial Sensors and Systems* (2019), pp. 1–12.
22. G. Sanders, L. Strandjord, J. Wu, W. Williams, M. Smiciklas, M. Salit, C. Narayanan, E. Benser, and T. Qiu, "Improvements of compact resonator fiber optic gyroscopes," in *DGON Inertial Sensors and Systems* (2017), pp. 1–12.
23. H. Ma, J. Zhang, L. Wang, and Z. Jin, "Double closed-loop resonant micro optic gyro using hybrid digital phase modulation," Opt. Express **23**, 15088–15097 (2015).
24. J. E. Heebner, V. Wong, A. Schweinsberg, R. W. Boyd, and D. J. Jackson, "Optical transmission characteristics of fiber ring resonators," IEEE J. Quantum Electron. **40**, 726–730 (2004).
25. G. B. Malykin, "Sagnac effect in ring lasers and ring resonators: how does the refractive index of the optical medium influence the sensitivity to rotation?" Phys. Usp. **57**, 714–720 (2014).
26. S. Zhao, Q. Liu, and Z. He, "White-light-driven resonant fiber-optic strain sensor," Opt. Lett. **45**, 5217–5220 (2020).
27. Z. Wang, Y. Yang, P. Lu, R. Luo, Y. Li, D. Zhao, C. Peng, and Z. Li, "Dual-polarization interferometric fiber-optic gyroscope with an ultra-simple configuration," Opt. Lett. **39**, 2463–2466 (2014).
28. W. J. Riley, *Handbook of Frequency Stability Analysis* (U.S. Department of Commerce/National Institute of Standards and Technology, 2008).
29. J. Davis and S. Ezekiel, "Closed-loop, low-noise fiber-optic rotation sensor," Opt. Lett. **6**, 505–507 (1981).
30. R. Meyer, S. Ezekiel, D. W. Stowe, and V. Tekippe, "Passive fiber-optic ring resonator for rotation sensing," Opt. Lett. **8**, 644–646 (1983).
31. W. Burns, R. Moeller, and A. Dandridge, "Excess noise in fiber gyroscope sources," IEEE Photon. Technol. Lett. **2**, 606–608 (1990).
32. Y. Zheng, H. Xu, J. Song, L. Li, and C. Zhang, "Excess relative-intensity-noise reduction in a fiber optic gyroscope using a Faraday rotator mirror," J. Lightwave Technol. **38**, 6939–6947 (2020).
33. J. Honthaas, J.-J. Bonnefois, E. Ducloux, and H. Lefèvre, "Interferometric filtering of the excess relative intensity noise of the broadband source of a fiber optic gyroscope," Proc. SPIE **9157**, 91572D (2014).
34. H. Zhang, X. Chen, X. Shu, and C. Liu, "Fiber optic gyroscope noise reduction with fiber ring resonator," Appl. Opt. **57**, 7391–7397 (2018).
35. A. Aleinik, I. Deineka, M. Smolovik, S. Neforosnyi, and A. Rupasov, "Compensation of excess RIN in fiber-optic gyro," Gyrosc. Navigation **7**, 214–222 (2016).
36. Z. Wang, Y. Yang, Y. Li, X. Yu, Z. Zhang, and Z. Li, "Quadrature demodulation with synchronous difference for interferometric fiber-optic gyroscopes," Opt. Express **20**, 25421–25431 (2012).
37. S. X.-Y. Huang, N. Sarma, K. M. Killian, and J. E. Goodwin, "Optical signal noise reduction for fiber optic gyroscopses," U.S. patent 5,898,496 (27 April, 1999).
38. W. Burns and R. Moeller, "Polarizer requirements for fiber gyroscopes with high-birefringence fiber and broad-band sources," J. Lightwave Technol. **2**, 430–435 (1984).
39. F. Mohr, "Thermooptically induced bias drift in fiber optical Sagnac interferometers," J. Lightwave Technol. **14**, 27–41 (1996).
40. Z. Li, Z. Meng, T. Liu, and X. S. Yao, "A novel method for determining and improving the quality of a quadrupolar fiber gyro coil under temperature variations," Opt. Express **21**, 2521–2530 (2013).